Editors' Suggestion | Featured in Physics

Imaging via Correlation of X-Ray Fluorescence Photons

Fabian Trost,[1,*] Kartik Ayyer,[2,3] Mauro Prasciolu,[1] Holger Fleckenstein,[1] Miriam Barthelmess,[1] Oleksandr Yefanov,[1] J. Lukas Dresselhaus,[3] Chufeng Li,[1] Saša Bajt,[1,3] Jerome Carnis,[1] Tamme Wollweber,[2,3] Abhishek Mall,[2] Zhou Shen,[2] Yulong Zhuang,[2] Stefan Richter,[4,5] Sebastian Karl,[4] Sebastian Cardoch,[6] Kajwal Kumar Patra,[6] Johannes Möller,[7] Alexey Zozulya,[7] Roman Shayduk,[7] Wei Lu,[7] Felix Braße,[7] Bertram Friedrich,[7] Ulrike Boesenberg,[7] Ilia Petrov,[7] Sergey Tomin,[8] Marc Guetg,[8] Anders Madsen,[7] Nicusor Timneanu,[6] Carl Caleman,[1,6] Ralf Röhlsberger,[3,9,10,11,8] Joachim von Zanthier,[4,5] and Henry N. Chapman[1,3,6,12,†]

[1]*Center for Free-Electron Laser Science CFEL, Deutsches Elektronen-Synchrotron DESY, Notkestr. 85, 22607, Hamburg, Germany*
[2]*Max Planck Institute for the Structure and Dynamics of Matter, 22607, Hamburg, Germany*
[3]*The Hamburg Centre for Ultrafast Imaging, Universität Hamburg, Luruper Chaussee 149, 22761 Hamburg, Germany*
[4]*Department of Physics, Friedrich-Alexander-Universität Erlangen-Nürnberg, Staudtstrasse 1, 91058 Erlangen, Germany*
[5]*Erlangen Graduate School in Advanced Optical Technologies (SAOT), Friedrich-Alexander Universität Erlangen-Nürnberg, Paul-Gordan-Str. 6, 91052, Erlangen, Germany*
[6]*Department of Physics and Astronomy, Uppsala University, Box 516, Uppsala SE-75120, Sweden*
[7]*European X-Ray Free-Electron Laser Facility, Holzkoppel 4, 22869 Schenefeld, Germany*
[8]*Deutsches Elektronen-Synchrotron DESY, Notkestr. 85, 22607 Hamburg, Germany*
[9]*Helmholtz-Institut Jena, Fröbelstieg 3, 07743 Jena, Germany*
[10]*GSI Helmholtzzentrum für Schwerionenforschung, Planckstrasse 1, 62491 Jena, Germany*
[11]*Institut für Optik und Quantenelektronik, Friedrich-Schiller-Universität Jena, Max-Wien-Platz 1, 07743 Jena, Germany*
[12]*Department of Physics, Universität Hamburg, Luruper Chaussee 149, 22761 Hamburg, Germany*

(Received 17 November 2022; revised 1 February 2023; accepted 8 March 2023; published 24 April 2023)

We demonstrate that x-ray fluorescence emission, which cannot maintain a stationary interference pattern, can be used to obtain images of structures by recording photon-photon correlations in the manner of the stellar intensity interferometry of Hanbury Brown and Twiss. This is achieved utilizing femtosecond-duration pulses of a hard x-ray free-electron laser to generate the emission in exposures comparable to the coherence time of the fluorescence. Iterative phasing of the photon correlation map generated a model-free real-space image of the structure of the emitters. Since fluorescence can dominate coherent scattering, this may enable imaging uncrystallised macromolecules.

DOI: 10.1103/PhysRevLett.130.173201

Introduction.—X-ray fluorescence provides identification of elements, whose distributions are usually mapped by scanning a focused x-ray or electron beam across a sample at a spatial resolution determined by the beam size [1]. Recently, a form of x-ray imaging was proposed that recovers the structure of fluorescing objects in a fundamentally different way, through the correlation of angularly resolved fluorescence counts [2]. Similar to intensity interferometry of Hanbury Brown and Twiss [3,4], structural information is revealed from the correlation of photons arriving in individual photodetectors (here, pixels of a million-element pixel-array detector). In the classical view, waves from independent emitters will interfere if they arrive at the detector and overlap within the coherence time of the emission τ_c, which is less than 1 fs for K-shell fluorescence from most elements. Using femtosecond-duration pulses from x-ray free-electron lasers, it becomes possible to excite fluorescence in atoms throughout a sample within a time comparable to τ_c, such that this interference can be observed without the need for a fast gating detector [2,5–7]. Unlike elastic scattering, where the phases of scattered waves have stationary phase relationships with each other that are dependent on the positions of the scatterers in three-dimensional space, the phases of the fluorescence waves have no such stationary relationship and fluctuate from pulse to pulse. The so-called intensity speckle patterns, $I(\vec{k})$, arising from this interference of waves with random phases, thus also differ from pulse to pulse. Here the wave vector of the emitted wave is defined with $|\vec{k}| = 1/\lambda$ for a wavelength λ. The sum of a large number of these patterns results in a uniform intensity, equivalent to

a long-exposure fluorescence measurement. Structural information can nevertheless still be recovered from the dataset by averaging photon-photon correlations over pairs of detector pixels, as

$$g^{(2)}(\vec{q}) = \frac{\langle I(\vec{k}) \cdot I(\vec{k}+\vec{q})\rangle_{\vec{k}}}{\langle I(\vec{k})\rangle_{\vec{k}}^2} = 1 + \beta |g^{(1)}(\vec{q})|^2 = 1 + \beta \frac{|F(\vec{q})|^2}{|F(0)|^2}, \quad (1)$$

an expression known as the Siegert relation [8]. The term $|g^{(1)}|$ is equal to the normalized magnitude of the Fourier transform F of the arrangement of the emitters, with a proportionality factor β that depends inversely on the number of coherent modes contributing to the measured intensities. This term $|g^{(1)}|$ provides information on the spatial frequencies of the emission distribution over a volume of reciprocal space subtended by all wave vector differences $\vec{q} = \vec{k}_1 - \vec{k}_2$ between pairs of detector pixels and hence extends to a spatial resolution dictated by the greatest angular separation of pixels in the detector (rather than on the largest scattering angle) [2]. An image of the real-space structure itself may then be obtained by a synthesis of the Fourier coefficients F, which, however, can only be achieved after retrieving the phases of these complex-valued terms. The solution of this "phase problem" has a long history in crystallography, and can usually be obtained directly for compact nonperiodic objects using iterative algorithms [9]. This method has been dubbed incoherent diffractive imaging [2] or fluorescence intensity correlation imaging [10].

In practice, this method of imaging faces the challenge that when sufficiently sampled, the detected intensity patterns $I(\vec{k})$ are only sparsely populated by photon counts. Furthermore, the signal to noise ratio (SNR) of $g^{(2)}$ decreases with increasing size and complexity of the emission structure [11]. Another difficulty is that the visibility factor β diminishes as the inverse of the duration of the excitation pulse relative to the fluorescence coherence time. The Kα emission from copper, used here, has a coherence time of $\tau_c = 0.6$ fs, given by twice the radiative lifetime $\hbar/\Gamma$ [8,12] for a spectral linewidth of $\Gamma = 2.17$ eV [13]. The reduction of β and the SNR due to these factors may require the recording of many millions of detector frames to obtain an interpretable map of $|g^{(1)}(\vec{q})|^2$, even for a simple structure. Since the SNR depends on the square of the peak intensity, this approach only becomes feasible with high-brightness pulsed sources such as x-ray free-electron lasers. So far, the use of fluorescence photon correlations has been successfully applied in the optical domain to characterize very small samples [14]. At x-ray energies, the method has been used to estimate the excitation pulse duration [5] and to determine the size of a focused x-ray beam illuminating a fluorescing foil [6]. In these two cases the number of emitters per real-space resolution element was large, and only the strength and width of the zero-order peak of $|g^{(1)}(\vec{q})|^2$ was determined, where the signal is high. Here, we demonstrate photon correlation imaging of a structured emission distribution of a Cu foil and give the first unequivocal demonstration that the method can be used to obtain a real-space image of a fluorescing structure in the x-ray domain.

Figure 1(a) illustrates the geometry of the experiment which was carried out at the MID instrument of the European XFEL [15]. X-ray free-electron laser (XFEL) pulses were generated with a nominal duration of 10 fs and a photon energy of 9.00 keV—just above the Cu K absorption edge. These were focused onto a 20 μm-thick Cu foil to generate fluorescence photons. The foil is thicker than the 3 μm length of a 10 fs incident pulse. Fluorescence is therefore generated in time as this pulse propagates through the thickness of the foil, which exits the rear 67 fs after it enters the front. Nevertheless, in the forward scattering direction, all generated fluorescence arrives nearly simultaneously at the detector, providing a coherence volume in the sample that is longer than the coherence length of the fluorescence [16]. The fluorescence in the forward direction was detected using an adaptive gain

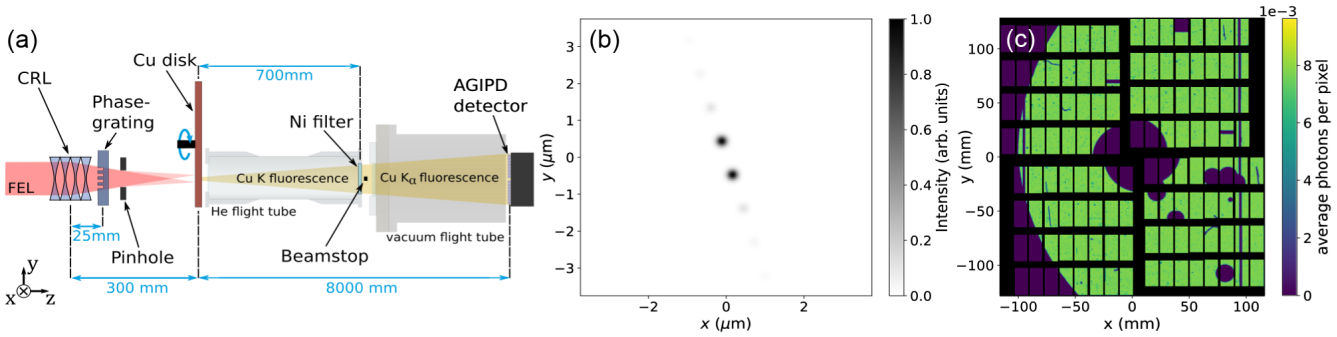

FIG. 1. (a) Simplified sketch of the experimental setup. (b) Simulated intensity distribution in the focal plane with the phase grating. (c) Photon counts at the AGIPD, measured with the phase grating, averaged over 58 million patterns. This is a flat distribution without any apparent structural information. The mean photon count per pixel per frame was $\langle I \rangle = 0.0077$.

integrating pixel detector (AGIPD) with one million pixels [17]. A Ni filter and a beamstop were used to block Cu Kβ radiation and elastic scattering from reaching the detector. The AGIPD was placed 8 m downstream of the emitting object to achieve sufficient angular resolution to sample speckle intensities arising from objects as big as 6 μm (see Supplemental Material [18]). This detector has single-photon sensitivity, and photon-photon correlations were computed between pairs of pixels not affected by shadows or elastic scattering. The detector is able to read 3520 frames per second, matched to the delivery of pulses from the XFEL. This capability, coupled with a scheme that moved a fresh area of Cu foil into the illumination on each pulse, allowed us to obtain a dataset with 58 million patterns, collected in less than 5 hours (see Appendix A).

To demonstrate the ability to recover a two-dimensional real-space image of a fluorescing structure, a pattern consisting predominantly of two 300 nm diameter spots separated by 860 nm was created by placing a diamond phase grating into the focused beam path as described in Appendix A. The calculated intensity distribution at the focal plane is shown in Fig. 1(b). When the Cu foil is located in this plane the fluorescence emission structure replicates the spot pattern.

Experiment.—Determination of the visibility factor β: The short-duration XFEL pulses were generated with a pulse energy of 150 μJ to 350 μJ. After transmission through the beamline and the focusing optics, the energy of the pulses impinging on the Cu foil ranged from 3 μJ to 7 μJ, or 2×10^9 to 5×10^9 photons, and the intensity in the focus exceeded 1×10^{18} W cm^{-2}. An average of 58 300 000 recorded AGIPD frames is shown in Fig. 1(c). Excluding shadows of the beamstop and entrance window, and masked regions of artifacts and bad pixels, the distribution of photon counts is relatively flat with a mean value of 0.0077 per pixel per pulse. This is comparable to 0.0063 photons per pixel estimated from the instrument detection efficiency and the production of fluorescence calculated from cold Cu cross sections. Some shadows of dust and debris can be discerned, likely on the Kapton entrance window downstream of the Cu disc. These features were excluded from the analysis. The number of pixels used in each detector frame to compute the correlations was 774 000.

To determine the visibility factor β of fluorescence photon correlations, and to first locate the focal plane, a single emission spot of 300 nm diameter was used by removing the diamond grating from the incident FEL beam. Since $g^{(2)}$ is proportional to the Fourier transform of the fluorescence emission, the best focus is found where the width of the correlation map is maximum (indicating the largest fluorescence speckle width, caused by the smallest transverse emitter distribution). A map of $g^{(2)}(\vec{q}) - 1$ obtained from 2 870 000 frames is shown in Fig. 2, at the longitudinal position z of the Cu foil that gave the largest correlation width (see Appendix B). A Gaussian fit of this map reveals an astigmatic focus with full widths at half maximum (FWHM) in two orthogonal directions of (640 ± 40) nm and (480 ± 30) nm, and a visibility $\beta = 0.018 \pm 0.002$.

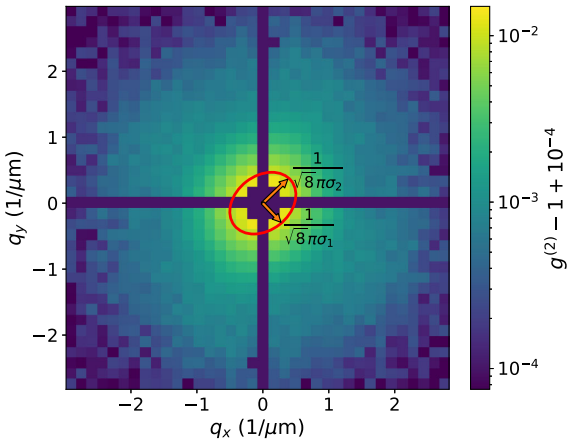

FIG. 2. $g^{(2)}$ signal of Cu Kα fluorescence with the Cu foil located in the focal plane ($z = 0$), without the phase grating. An offset of 1×10^{-4} was added for the logarithmic representation. The rms width of a fitted Gaussian is marked, with $\sigma_1 = (272 \pm 17)$ nm and $\sigma_2 = (204 \pm 13)$ nm. See Appendix B for details.

The visibility factor gives the inverse of the number of participating modes. It can thus be used to estimate the pulse duration T, relative to the coherence time. Accounting for the polarization states of the fluorescence photons and the presence of Kα_1 and Kα_2 emission, we find $\beta \approx 5\tau_c/(27T)$ (see Appendix B). Given $\tau_c = 0.6$ fs, we therefore obtain an effective FWHM pulse duration (for a Gaussian pulse shape) of $T = (6.2 \pm 0.8)$ fs.

Imaging of a fluorescing structure: Detector frames, recording emission from predominantly two separated spots as indicated by Fig. 1(b), were obtained with the phase grating inserted in the incident XFEL beam. The expected $g^{(2)}$ signal, given this emission structure and a visibility of $\beta = 0.018$, is presented in Appendix A, Fig. 4. This $g^{(2)}$ map is dominated by a fringe pattern, as one would expect from the interference of light from two sources, yet revealed in this case only in the photon-photon correlations to give the square modulus of the Fourier transform of the emission structure [Eq. (1)]. The orientation of the grating bars in the experiment, and in this calculation, was set to be 17° from horizontal to avoid producing a signal that modulates in a direction parallel to detector rows or columns (which may give false correlations due to detector common modes).

The experimental $g^{(2)} - 1$ signal, obtained from 58 million recorded frames, is displayed in Fig. 3(a) on a logarithmic scale (an offset of 1×10^{-4} was added for this representation). It shows a fringe pattern that is comparable to the predicted pattern. Fringes to the third order can be discerned, showing that the signal extends to $|q| \approx 4$ μm^{-1}.

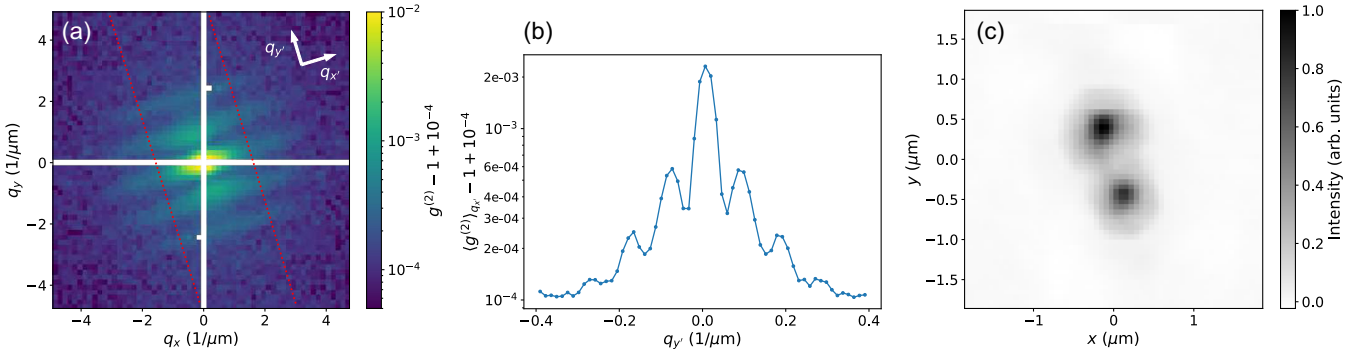

FIG. 3. (a) Measured $g^{(2)} - 1$ signal in logarithmic representation. (b) Cut through the $g^{(2)} - 1$ signal along $q_{y'}$ and integrated along $q_{x'}$ within the boundaries indicated in (a). The distance between the boundaries was optimized to achieve maximum fringe visibility. (c) Reconstructed fluorescence emitter distribution at the Cu disk, to be compared with the simulation in Fig. 1(b).

The rms of the background is measured at 3.52×10^{-5}, which can be considered the noise floor. A projection of the $g^{(2)} - 1$ signal is shown in Fig. 3(b) along the direction of the grating modulation [summing pixels between the red dashed lines in Fig. 3(a)].

An image of the fluorescing structure cannot be obtained from the Fourier magnitude of the structure alone, but requires knowledge of the Fourier transform phase map, which is not provided by the $g^{(2)}$ measurement. We obtained this via iterative phase retrieval [9], by constraining the image to be the most compact structure consistent with the Fourier magnitudes $|F(\vec{q})|$ determined from the map given in Fig. 3(a). We carried out phasing using the "Shrinkwrap" algorithm [23] (see Supplemental Material [18]). The reconstructed image of the fluorescing structure, obtained by averaging 1000 phase retrieval trials, is shown in Fig. 3(c). It shows two well-resolved diffraction spots of the grating, one slightly more intense than the other. Each spot has a FWHM of about 400 nm.

Discussion.—The results depicted in Fig. 3 indicate the feasibility of imaging via the correlation of hard x-ray fluorescence photons, as recently proposed by Classen *et al.* [2]. In the classical view, photons emitted from independent atoms generate measurable interference if their arrival at the detector coincides within the coherence time of those photons. Unlike the intensity interferometry of Hanbury Brown and Twiss, which relies upon selecting a narrow bandwidth of the thermal radiation to provide a coherence time comparable to the detector response time, we achieve this by generating the fluorescence with femtosecond-duration XFEL pulses. In this first demonstration of the method the pulse duration was about ten times longer than the 0.6 fs coherence time of Cu Kα radiation, resulting in the incoherent addition of more than 50 coherent modes in each measurement (accounting for polarization and the emission spectrum). The number of detected photons per pixel per mode was thus $\mu = \langle I \rangle / 50 = 1.5 \times 10^{-4}$, generated by about 1.2×10^8 incident x-ray photons per mode (200 nJ). Future compact subfemtosecond x-ray sources may produce similar numbers of photons per mode [24–26].

Since the method is based upon photon-photon correlations, the SNR of the $g^{(2)}$ estimate scales favorably with increasing measured signals μ and with a reduction of the number of participating modes per measurement [11,27]. Large reductions in the required number of frames, which scales as $1/\mathrm{SNR}^2$, could therefore be obtained with modest improvements in source properties. The SNR scales approximately linearly with contrast β, or inversely with the number of modes [11]. High-brightness attosecond-duration photon sources [28] could achieve parity of the coherence and detection times (five coherent modes), to accomplish an equivalent SNR with fewer measurements by a factor of $1/10^2$ (i.e., 580000 frames collected in three minutes), for the same 1.2×10^8 incident photons per coherence mode as used here—that is, for the same incident power of approximately 1 GW. Additional gains could be achieved by increasing power. For example, a 1 TW incident pulse (0.6 mJ in 0.6 fs) would provide 0.18 photons/pixel/mode, 1000 times more than achieved here, giving an increase in the SNR by this same factor (depending on the shape of the object [11]) and thus requiring only $1/1000^2$ of the number of measurements. Multiple detectors could be placed to record the isotropic x-ray fluorescence to increase the number of detected photons per shot, as well as the number of potential photon-photon correlations. This will provide a corresponding increase of the SNR [11] as well as the potential to increase resolution to a limit of $\lambda/2$ with detectors arranged in opposing directions [2]. Together, all these factors would allow similar results as achieved here with only tens of pulses. Indeed, when signals of this level are obtained in million-pixel detectors the number of photon-photon correlations that can be computed exceeds 10^{10}. Analyses of several groups [2,10,11,16,27] indicate the possibility to extract reasonable $g^{(2)}$ measurements in such situations.

A limitation of the incident pulse fluence is given by the saturation of photoabsorption. Since fluorescence at an equivalent energy cannot occur more than once per atom during the coherence time, fluorescence will statistically fully saturate above $I_0 = h\nu/(\sigma_A \tau_c)$, where σ_A is the photoabsorption cross section. For Cu at 9 keV photon energy, $\sigma_A = 2.92 \times 10^{-20}$ cm^2 per atom, giving a limit of $I_0 = 1 \times 10^{20}$ W cm^{-2}, equivalent to the example with a 1 TW incident pulse given above.

Based on our results and these scalings, incoherent diffractive imaging via correlation of x-ray fluorescence photons should therefore be feasible to rapidly monitor the focal distribution [6] and pulse duration [5] of intense x-ray beams, as well as to obtain high-resolution three-dimensional images of fluorescing structures for the real-time analysis of the formation and evolution of dense plasmas (e.g., in plasma physics and fusion energy research [10,29]). Our results are also consistent with predictions to image clusters and single molecules at atomic resolution [2,10,11]. The small dimensions of such objects substantially relax the detector angular resolution, making it practical to record fluorescence over large solid angles with current pixel-array detectors, thereby providing atomic resolution. Unlike elastic scattering, where atomic scattering factors fall precipitously with scattering angle and require ever greater exposures to increase spatial resolution, fluorescence is emitted uniformly in all directions. Therefore, the imaging of atomic structures does not necessarily require higher intensities than discussed here, but may require a similar number of patterns as here ($\sim 10^7$). Diffraction measurements of single particles or macromolecules [30,31] could be readily combined with simultaneous fluorescence measurements, which themselves could be extended to discriminate fluorescence photons over a wide spectral range, to image substructures which could be used to track charge transfer or progression of oxidation states in the biocomplexes of photosynthesis [32] or other catalytic systems.

We acknowledge European XFEL in Schenefeld, Germany, for provision of x-ray free-electron laser beamtime at the MID instrument on the SASE-2 beamline and would like to thank the staff for their assistance. This research was supported by DESY (Hamburg, Germany), a member of the Helmholtz Association HGF; the Cluster of Excellence 'Advanced Imaging of Matter' of the Deutsche Forschungsgemeinschaft (DFG)–EXC 2056–Project ID No. 390715994; and the Initiative and Networking Funds of the Helmholtz Association through ExNet-0002 "Advanced Imaging of Matter." Maxwell computational resources were provided by DESY (Hamburg, Germany). S. C., K. K. P., N. T., and C. C. thank the Swedish Research Council (Grants No. 2018-00740 and No. 2019-03935) and the Carl Tryggers Foundation (Grant No. CTS 18:392) for financial support. S. R., S. K., Jv. Z., and R. R. thank the Deutsche Forschungsgemeinschaft (DFG, German Research Foundation) within the TRR 306 QuCoLiMa ("Quantum Cooperativity of Light and Matter")–Project-ID No. 429529648 for financial support. Data recorded for the experiment at the European XFEL are available at doi: 10.22003/XFEL.EU-DATA-002841-00.

Appendix A: Fluorescence generation.—X-ray fluorescence was generated in a 20 μm-thick Cu foil by excitation with femtosecond-duration x-ray pulses. These XFEL pulses were focused to a 300 nm spot using two sets of compound refractive lenses (CRLs) in series with an effective diameter of 300 μm and a combined focal length of 300 mm. When placed into this focus, the Cu foil is damaged by a single pulse, which creates a crater. Repeated exposures quickly produced a hole bigger than the focused beam, up to about 15 μm in diameter. Therefore the foil must be moved to a fresh area after each exposure. The FEL pulses were produced in trains within which pulses were separated by 444 ns (2.25 MHz repetition), so the foil must exceed 30 m s^{-1}, a speed that was achieved using a spinning foil disc. This disc, of 150 mm diameter, was mounted on a spoked aluminum frame and spun at rates of up to 4500 rpm. The precise speed was chosen so that the location of the first pulse in a train would impact the foil just beyond the angular position of the last pulse of the previous train. By slowly translating the spinning foil in a direction transverse to the beam a single foil could last for many hours with 10 pulse trains per second and 352 pulses per train. This number matches the frame capacity of the AGIPD.

To produce the structured emission profile to be imaged, a phase transmission grating, milled into a 42 μm-thick diamond wafer, could be inserted 25 mm downstream of the principal plane of the second lens stack to produce a series of diffracted orders in the focal plane. The grating period was 80 μm and consisted of equal-width bars of alternating heights differing by 8.4 μm to give a π phase difference at a photon energy of 9.0 keV. The complex transmissions of the bars were thus 1 and -1, producing dominant ± 1 orders without any zero order, separated by 860 nm in the focal plane. The calculated intensity distribution is shown in Fig. 1(b), and the resulting simulated $g^{(2)}$ signal is displayed in Fig. 4.

Assuming the cold transmission, 20 μm of Cu absorbs 99.4% of the incident beam. The generation and transmission of the fluorescence depends on the depth in the foil in which it is generated, and it is expected that 5×10^9 incident photons results in an emission of 8.4×10^7 fluorescent photons per steradian in the forward direction.

Appendix B: Locating best focus and determining the visibility factor β.—In the classical limit, the origin of the $g^{(2)}(0) - 1 = \langle I(\vec{k})^2 \rangle / \langle I(\vec{k}) \rangle^2 - 1$ map should reveal the visibility factor β. With low photon counts, however, the expected value diverges [7,11] and does not give a reliable analysis. In addition, this value is overly

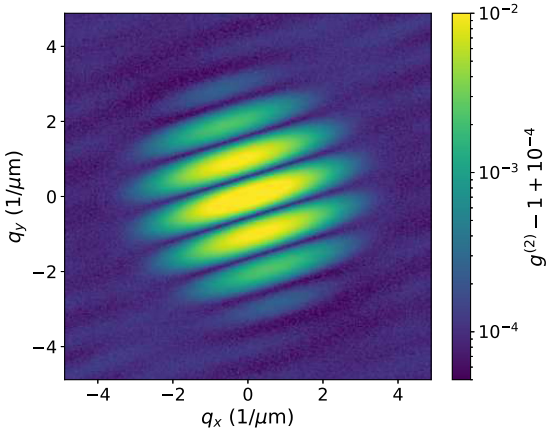

FIG. 4. Simulated $g^{(2)} - 1$ signal for the intensity distribution displayed in Fig. 1(b) with an assumed visibility of $\beta = 0.018$.

sensitive to background as compared with other values of $\vec{q}$, due to elastically scattered photons and detector noise. Moreover, the computation of $g^{(2)}$ along the horizontal and vertical axes ($q_x = 0$ and $q_y = 0$) suffers from false correlations along particular readout rows and columns of the detector (so-called common mode artifacts). Additionally, charge sharing between neighboring pixels confounds measurements at $(q_x, q_y) = (\pm 1, \pm 1)$. Approximating the CRL focus by a Gaussian, we determined β from a fit of the function $\beta \exp(-4\pi^2(q_1^2\sigma_1^2 - q_2^2\sigma_2^2))$ to the map in Fig. 2. Here, (q_1, q_2) form a basis rotated by 38° to (q_x, q_y) to account for an apparent astigmatism of the focus. Given that $|g^{(1)}|$ is proportional to the Fourier transform of the fluorescence emission, this fit gives a focus size of $\mathrm{FWHM}_1 = (640 \pm 40)$ nm, $\mathrm{FWHM}_2 = (480 \pm 30)$ nm, and a visibility of $\beta = 0.018 \pm 0.002$. A plot of the inverse of the focal area, $1/(\sigma_1\sigma_2)$, determined this way is shown in Fig. 5, for displacements z of the foil along the beam axis. The focus (at $z = 0$) can be clearly discerned. The fitted visibility factor at each position, also displayed in the plot, is approximately uniform over the defocus range.

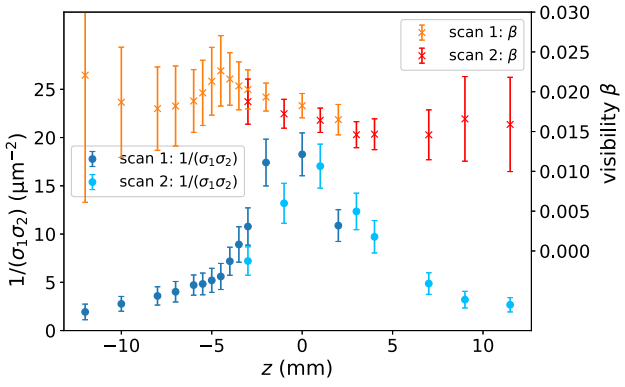

FIG. 5. Inverse of the focal area $1/(\sigma_1\sigma_2)$, and the fitted visibility β, versus defocus z. The data were measured during two different scans.

The visibility factor gives the inverse of the number of participating modes. It can thus be used to estimate the pulse duration T relative to the coherence time. In particular

$$\beta = \frac{1}{2}\int_{-\infty}^{\infty} \Pi(\tau)|\gamma(\tau)|^2 d\tau \approx \frac{1}{3}\frac{\tau_c}{T}, \tag{B1}$$

where $\Pi(\tau) = \langle P(t)P(t+\tau)\rangle / \langle P(t)\rangle^2$ denotes the normalized autocorrelation of the excitation pulse intensity $P(t)$ and γ is the complex degree of coherence of the fluorescence [8,13]. The factor $1/2$ in Eq. (B1) appears since the detector does not discriminate the polarization states of the fluorescence photons. The approximation to Eq. (B1) is obtained for a Gaussian excitation with a FWHM pulse duration T, where $P(t) \propto \exp(-4\log(2)t^2/T^2)$, and $|\gamma(\tau)|^2 = \exp(-2|\tau|/\tau_c)$. Our measurements do not discriminate $\mathrm{K}\alpha_1$ and $\mathrm{K}\alpha_2$ emission, and thus they will contribute as mutually incoherent modes. The branching ratios for the K-shell are $R_{\mathrm{K}_{\alpha,1}} = 0.581$ and $R_{\mathrm{K}_{\alpha,2}} = 0.297$ [33], respectively, so Eq. (B1) must be adjusted by the factor $R_{\mathrm{K}_{\alpha,1}}^2/(R_{\mathrm{K}_{\alpha,1}} + R_{\mathrm{K}_{\alpha,2}})^2 + R_{\mathrm{K}_{\alpha,2}}^2/(R_{\mathrm{K}_{\alpha,1}} + R_{\mathrm{K}_{\alpha,2}})^2 \approx 5/9$ [27], resulting in

$$\beta \approx \frac{5\tau_c}{27T}. \tag{B2}$$

Given $\tau_c = 0.6$ fs, we therefore obtain an effective FWHM pulse duration (for a Gaussian pulse shape) of $T = (6.2 \pm 0.8)$ fs.

Correlation maps at different displacements z were obtained by recording frames at each position, made during two separate scans of the z position of the nanofocusing CRL stack as shown in Fig. 5. The number of recorded frames per z position was 3 000 000 (20 minutes per position) for scan 1 and 1 500 000 for scan 2 (10 minutes per position). However, due to detector failures some positions in scan 2 were recorded with only about 750 000 frames. The plot in Fig. 5 depicts the inverse of the focal area, $1/(\sigma_1\sigma_2)$ obtained from these maps, along with the fitted visibility factor at each position. The focus can be clearly discerned, with a beam area varying quadratically with defocus distance z, consistent with a numerical aperture of 0.5×10^{-3}. The first scan (scan 1) was made prior to the insertion of 42 μm thickness of diamond in the converging beam (the substrate of the phase grating), and the second (scan 2) was made with the diamond. Even though the flat diamond should have little effect, a slight shift of the focus was observed. The estimate of the visibility (and hence the pulse duration) is approximately uniform over the defocus range, although higher precision is achieved near the focus.

*fabian.trost@desy.de
†henry.chapman@desy.de

[1] V. V. Lider, Phys. Usp. **61**, 980 (2018).
[2] A. Classen, K. Ayyer, H. N. Chapman, R. Röhlsberger, and J. von Zanthier, Phys. Rev. Lett. **119**, 053401 (2017).
[3] R. Q. Twiss, Opt. Acta **16**, 423 (1969).
[4] R. Hanbury Brown, Annu. Rev. Astron. Astrophys. **6**, 13 (1968).
[5] I. Inoue, K. Tamasaku, T. Osaka, Y. Inubushi, and M. Yabashi, J. Synchrotron Radiat. **26**, 2050 (2019).
[6] N. Nakamura, S. Matsuyama, T. Inoue, I. Inoue, J. Yamada, T. Osaka, M. Yabashi, T. Ishikawa, and K. Yamauchi, J. Synchrotron Radiat. **27**, 1366 (2020).
[7] F. Trost, K. Ayyer, D. Oberthuer, O. Yefanov, S. Bajt, C. Caleman, A. Weimer, A. Feld, H. Weller, S. Boutet *et al.*, J. Synchrotron Radiat. **30** (2023).
[8] J. W. Goodman, *Statistical Optics (Wiley Series in Pure and Applied Optics)* (Wiley-Interscience, New York, 1985).
[9] Y. Shechtman, Y. Eldar, O. Cohen, H. Chapman, J. Miao, and M. Segev, Signal Proc. Mag., IEEE **32**, 87 (2015).
[10] P. J. Ho, C. Knight, and L. Young, Struct. Dyn. **8**, 044101 (2021).
[11] F. Trost, K. Ayyer, and H. N. Chapman, New J. Phys. **22**, 083070 (2020).
[12] H. E. White *et al.*, *Introduction to Atomic Spectra* (McGraw-Hill book Co., Inc., New York, 1934).
[13] M. O. Krause and J. H. Oliver, J. Phys. Chem. Ref. Data **8**, 329 (1979).
[14] S. Richter, S. Wolf, J. von Zanthier, and F. Schmidt-Kaler, Phys. Rev. Lett. **126**, 173602 (2021).
[15] A. Madsen, J. Hallmann, G. Ansaldi, T. Roth, W. Lu, C. Kim, U. Bösenberg, A. Zozulya, J. Möller, R. Shayduk *et al.*, J. Synchrotron Radiat. **28**, 637 (2021).
[16] A. S. H. Shevchuk, J. C. H. Spence, R. A. Kirian, W. S. Graves, and K. E. Schmidt, Phys. Rev. A **104**, 023514 (2021).
[17] A. Allahgholi *et al.*, J. Synchrotron Radiat. **26**, 74 (2019).
[18] See Supplemental Material at http://link.aps.org/supplemental/10.1103/PhysRevLett.130.173201 for fluorescence detection and phase retrieval, which includes Refs. [19–22].
[19] J. R. Fienup, Appl. Opt. **21**, 2758 (1982).
[20] V. Elser, J. Opt. Soc. Am. A **20**, 40 (2003).
[21] J. R. Fienup, Appl. Opt. **36**, 8352 (1997).
[22] D. Shapiro, P. Thibault, T. Beetz, V. Elser, M. Howells, C. Jacobsen, J. Kirz, E. Lima, H. Miao, A. M. Neiman *et al.*, Proc. Natl. Acad. Sci. U.S.A. **102**, 15343 (2005).
[23] S. Marchesini, H. He, H. N. Chapman, S. P. Hau-Riege, A. Noy, M. R. Howells, U. Weierstall, and J. C. H. Spence, Phys. Rev. B **68**, 140101(R) (2003).
[24] F. X. Kärtner, F. Ahr, A.-L. Calendron, H. Cankaya, S. Carbajo *et al.*, Nucl. Instrum. Methods Phys. Res., Sect. A **829**, 24 (2016).
[25] W. Graves, J. Chen, P. Fromme, M. Holl, R. Kirian, L. Malin, K. Schmidt, J. Spence, M. Underhill, U. Weierstall *et al.*, in *Proceedings of the 38th International Free-Electron Laser Conference (FEL 2017)*, edited by K. Bishofberger, B. Carlsten, and V. R. W. Schaa, (JACoW, 2018), p. TUB03.
[26] J. B. Rosenzweig, N. Majernik, R. R. Robles, G. Andonian, O. Camacho *et al.*, New J. Phys. **22**, 093067 (2020).
[27] L. M. Lohse, M. Vassholz, and T. Salditt, Acta Crystallogr. Sect. A **77**, 480 (2021).
[28] Y. W. Parc, C. H. Shim, and D. E. Kim, Appl. Sci. **8** (2018).
[29] L. B. Fletcher *et al.*, Nat. Photonics **9**, 274 (2015).
[30] R. Neutze, R. Wouts, D. van der Spoel, E. Weckert, and J. Hajdu, Nature (London) **406**, 753 (2000).
[31] M. M. Seibert, T. Ekeberg, F. R. N. C. Maia, M. Svenda, J. Andreasson *et al.*, Nature (London) **470**, 78 (2011).
[32] M. Suga, A. Shimada, F. Akita, J.-R. Shen, T. Tosha, and H. Sugimoto, Biochim. Biophys. Acta **1864**, 129466 (2020).
[33] A. Brunetti, M. Sanchez del Rio, B. Golosio, A. Simionovici, and A. Somogyi, Spectrochim. Acta B Atom. Spectros. **59**, 1725 (2004).